BNL-107535-2015-JA

Structure-Based Functional Characterization of Repressor of Toxin (Rot), a Central Regulator of Staphylococcus aureus Virulence

April Killikelly[1, a], Meredith A. Benson[2, a], Elizabeth A. Ohneck[2, a], Jared M. Sampson[1], Jean Jakoncic[3], Brett Spurrier[1], Victor J. Torres[2, *] and Xiang-Peng Kong[1,*]

Departments of [1]Biochemistry and Molecular Pharmacology and [2]Microbiology, NYU School of Medicine, New York, NY 10016, USA.
[3]Photon Sciences Directorate, Brookhaven National Laboratory, Upton, NY 11973 USA.

Submitted to Journal of Bacteriology

January 2015

National Synchrotron Light Source II

Brookhaven National Laboratory

U.S. Department of Energy
[DOE – Office of Science]

Notice: This manuscript has been co-authored by employees of Brookhaven Science Associates, LLC under Contract No. DE-SC0012704 with the U.S. Department of Energy. The publisher by accepting the manuscript for publication acknowledges that the United States Government retains a non-exclusive, paid-up, irrevocable, world-wide license to publish or reproduce the published form of this manuscript, or allow others to do so, for United States Government purposes.

DISCLAIMER

This report was prepared as an account of work sponsored by an agency of the United States Government. Neither the United States Government nor any agency thereof, nor any of their employees, nor any of their contractors, subcontractors, or their employees, makes any warranty, express or implied, or assumes any legal liability or responsibility for the accuracy, completeness, or any third party's use or the results of such use of any information, apparatus, product, or process disclosed, or represents that its use would not infringe privately owned rights. Reference herein to any specific commercial product, process, or service by trade name, trademark, manufacturer, or otherwise, does not necessarily constitute or imply its endorsement, recommendation, or favoring by the United States Government or any agency thereof or its contractors or subcontractors. The views and opinions of authors expressed herein do not necessarily state or reflect those of the United States Government or any agency thereof.

Structure-based functional characterization of Repressor of Toxin (Rot), a central regulator of *Staphylococcus aureus* virulence

April Killikelly[1, a], Meredith A. Benson[2, a], Elizabeth A. Ohneck[2, a], Jared M. Sampson[1], Jean Jakoncic[3], Brett Spurrier[1], Victor J. Torres[2, *] and Xiang-Peng Kong[1,*]

Departments of [1]Biochemistry and Molecular Pharmacology and [2]Microbiology, NYU School of Medicine, New York, NY 10016, USA. [3]Photon Sciences Directorate, Brookhaven National Laboratory, Upton, NY 11973 USA.

[a] contributed equally to this work.

Running title: Structural-functional analysis of Rot

[*] Send correspondences to: Xiangpeng.Kong@med.nyu.edu and Victor.Torres@nyumc.org

Keywords: *Staphylococcus aureus;* Repressor of Toxin (Rot); Crystal structure; Winged-Helix-Turn-Helix (WHTH); Site-directed mutagenesis

ABSTRACT

Staphylococcus aureus is responsible for a large number of diverse infections worldwide. In order to support its pathogenic lifestyle, *S. aureus* has to regulate the expression of virulence factors in a coordinated fashion. At the center of the *S. aureus* regulatory networks is the transcription factor Repressor of Toxins (Rot). Rot plays a key role in regulating *S. aureus* virulence through activation or repression of promoters that control expression of a large number of critical virulence factors. However, the mechanism by which Rot-mediates gene regulation has remained elusive. Here, we have we determined the crystal structure of Rot and used this information to probe the contribution made by specific residues to Rot function. Rot was found to form a dimer, with each monomer harboring a Winged-Helix-Turn-Helix (WHTH) DNA binding motif. Despite an overall acidic pI, the asymmetric electrostatic charge profile suggests that Rot can orient the WHTH domain to bind DNA. Structure-based site-directed mutagenesis studies demonstrated that R^{91}, at the tip of the wing, plays an important role in DNA-binding, likely through interaction with the minor groove. We also found that Y^{66}, predicted to bind within the major groove, contributes to Rot interaction with target promoters. Evaluation of Rot binding to different activated and repressed promoters revealed that certain mutations on Rot exhibit promoter-specific effects, suggesting for the first time that Rot differentially interacts with target promoters. This work provides insight into a precise mechanism by which Rot controls virulence factor regulation in *S. aureus*.

39 **INTRODUCTION**

40 *Staphylococcus aureus,* a leading cause of hospital acquired infections, is an opportunistic
41 Gram-positive pathogenic bacterium able to infect diverse body tissues and manifest in a
42 variety of disease states such as osteomyelitis, endocarditis, sepsis and toxic shock
43 syndrome, among others (1-3). *S. aureus* has adapted to circumvent therapeutic strategies
44 by developing resistance to antibiotics (4, 5). These resistant strains were initially
45 observed in hospital settings, but are now prevalent in the community, infecting otherwise
46 healthy individuals (6). The ability of *S. aureus* to evolve in response to therapeutic efforts
47 has resulted in strains resistant to vancomycin, which was previously used as a drug of last
48 resort (7). Thus, this versatile pathogen presents a great challenge to human health,
49 creating an urgent need for the development of new therapeutics to combat infections.

50

51 *S. aureus* can modify gene transcription for optimal pathogenesis by way of temporal
52 control of virulence factors in response to quorum sensing via the accessory gene
53 regulatory system (Agr) (8-10). The receptor kinase of the Agr two-component system
54 (TCS), AgrC, is engaged by the auto-inducing peptide AIP, the extracellular concentration of
55 which is proportional to the density of the bacteria within a certain radius. AgrC, in turn,
56 activates the response regulator, AgrA, to regulate target genes (11). Once a concentration
57 threshold of AIP is reached, usually at late exponential phase, Agr is activated, altering
58 virulence factor expression (9). Activation of Agr results in the upregulation of a regulatory
59 RNA molecule known as RNAIII (12-14). This molecule interacts with target mRNAs,
60 resulting in either degradation of the transcript or exposure of the Shine-Delgarno
61 sequence and increased translation (14-18). One of the most well-characterized targets of

62 RNAIII is the SarA family member repressor of toxins (Rot) (15, 16, 19). Interaction of
63 RNAIII with *rot* mRNA results in degradation of the transcript and a reduction of Rot in the
64 bacteria (15, 16), leading to changes in virulence factor expression, including the down-
65 regulation of cell wall-associated proteins (including protein A, fibrinogen and fibronectin
66 binding proteins) and up-regulation of secreted factors (such as hemolysins and proteases)
67 (19, 20). By way of this system, *S. aureus* is thought to synchronize its patterns of virulence
68 expression on a population-wide scale during infection (9, 21).
69
70 Rot was originally identified in a transposon screen as a repressor of *hla*, which encodes
71 the α-Toxin (19). Mutation of the *rot* locus is associated with increased virulence in a rabbit
72 endocarditis model of infection and in a murine bacteremia model (22, 23). Transcriptional
73 profiling studies demonstrated that Rot regulates 146 genes, serving as a repressor of 60
74 and an activator 86 (20). Rot is known to have direct and specific interactions with several
75 target promoters to regulate gene expression, notably those of *hla* (20, 22), *ssl7*, which
76 encodes a staphylococcal superantigen-like protein (24), and *seb*, encoding enterotoxin B
77 (25). Importantly, Rot can act as either an activator or a repressor of target promoters,
78 activating genes such as *ssl7* and *spa*, encoding staphylococcal protein A, and repressing
79 genes such as *hla* and *lukED*, which encodes a pore-forming toxin. However, how Rot
80 differentiates amongst these promoters is not known.
81
82 Rot is a member of the SarA family of transcription regulators (26). The SarA family was
83 first identified by sequence-based homology studies, with all family members containing a
84 conserved sequence motif KxRxxxDER (26). Previous sequence and structural analyses of

85 several family members have shown that all possess a Winged-Helix-Turn-Helix (WHTH)
86 domain, a variation of the classical DNA-binding Helix-Turn-Helix (HTH) motif (27). The
87 prototypic members of the HTH family are the well-known λ-phage proteins Cro and the
88 catabolite activator protein (CAP) from *E. coli*, in which the C-terminal Recognition Helix
89 (RH) was demonstrated to project into the major groove of DNA (28-30). Further
90 structure-based analyses classified SarA family members into three groups: (i) single-
91 domain structures (SarA, SarR, SarT, SarV, SarX, and Rot), (ii) two-domain structures (SarS,
92 SarU and SarY), and (iii) single domain structures that are highly homologous to the MarR
93 family (SarZ, MgrA and homologues) (26).
94
95 Rot is a unique member of the SarA family because it has a very acidic sequence and does
96 not contain any cysteine residues (26). The aim of this work was to combine structural and
97 functional analyses to uncover the molecular means of Rot-mediated regulation. To this
98 end, we determined a crystal structure of Rot and used this information to predict residues
99 involved in DNA binding. Construction and characterization of mutants to probe the
100 contribution made by specific residues resulted in identification of key residues necessary
101 for Rot binding and function. Our results provide important insights into how Rot is able to
102 orient itself to DNA, and bind to and make selective contact with specific promoters.
103
104 **MATERIALS AND METHODS**
105 **Bacterial strains and culture conditions.** Strains used in this study are described in
106 Table 4. *S. aureus* strains were grown at 37°C with shaking at 180 rpm in tryptic soy broth
107 (TSB) or in Roswell Park Memorial Institute medium (RPMI) supplemented with 1% CAS

108 amino acids (RPMI/CAS). When indicated, TSB and RPMI were supplemented with
109 chloramphenicol (Cm) to a final concentration of 10 μg/mL. *E. coli* DH5α were grown in
110 Luria-Bertani (LB) broth at 37°C with shaking at 180 rpm. When necessary, LB was
111 supplemented with ampicillin (Amp) to a final concentration of 100 μg/mL.
112
113 **Rot Production.** Recombinant Rot protein was produced as previously described by
114 Benson *et al* (31). Briefly, the *rot* gene with additional C-terminal His-tag was cloned into
115 the pET41b expression vector and was transformed into the *E. coli* expression strain T7
116 *lysY*/I^q (NEB). To produce a selenomethionine derivative, cells were initially grown in a
117 mixture of Base, Nutrient Mix, Methionine (Molecular Dimensions) and antibiotics at 37°C
118 with shaking at 220 rpm until the cell density reached an A_{600} of 0.8. Cells were isolated by
119 centrifugation at 5000 rpm, washed with media and resuspended in a mixture of Base,
120 Nutrient Mix, Selenomethionine (Molecular Dimensions) and antibiotics. Protein
121 expression was induced with IPTG for 3 hours. Cells were collected from the medium by
122 centrifugation at 5000 rpm and resuspended in Tris-buffered saline (TBS) supplemented
123 with 10 mM Imidazole and an EDTA-free protease inhibitor, and then lysed by sonication
124 on ice. Soluble proteins were isolated from cellular debris by centrifugation at 15,000 rpm.
125 The recombinant Rot protein was further purified by Ni-NTA chromatography and eluted
126 with 500 mM Imidazole.
127
128 **Crystallization, Data Collection, Structure Determination, and Refinement.** Purified
129 Rot protein was assayed by size exclusion chromatography for purity and homogeneity.
130 Native and selenomethione-labeled (SeMet) Rot proteins were concentrated to 6 and 2.5

131 mg/mL for crystallization, respectively. Both native and SeMet crystals were obtained by
132 hanging drop vapor diffusion over reservoirs containing 10% PEG 6K, 0.7 M LiCl and 0.2 M
133 Citric Acid pH 5. Single crystals were briefly soaked in the mother liquor supplemented
134 with 20% MPD (v/v) prior to being flash cooled in liquid nitrogen. Both native and MAD
135 diffraction data were collected at beamline X6A, National Synchrotron Light Source,
136 Brookhaven National Laboratory. The native dataset was collected from a single crystal at a
137 wavelength of 1.0 Å. All three MAD datasets were collected from a single SeMet crystal at
138 energies of 12656 eV (inflection point), 12661 eV (peak) and 13580 eV (high energy
139 remote), based on a fluorescence scan of the Se absorption *K* edge. All four datasets were
140 comprised of 360 images collected in a stream of gaseous nitrogen at 100 K and with a 1°
141 oscillation for each frame. Full data-collection statistics are given in Table 1. Each data set
142 was processed separately, first integrated using iMosflm (32), then merged and scaled
143 using POINTLESS and SCALA from the CCP4 suite (33). The 3 MAD datasets were combined
144 using CAD and normalized using Scaleit in CCP4 (34). The SHELXCDE set of programs (35)
145 was used to determine the selenium substructure and calculate the initial phase; a model
146 was built into the resultant electron density using BUCCANEER (36) in CCP4. This initial
147 MAD-phased model was improved by alternating cycles of real space fitting and restrained
148 refinement against the native dataset using Coot (37) and Refmac5 (38), using
149 automatically generated NCS restraints. Final restrained refinement was done with PHENIX
150 Refine (39). Structural figures were generated using PyMOL (40) and ICM (41). Buried
151 surface area and dimerization calculations were done with the PISA server (42).
152

153 **Generation of site-directed Rot mutants.** Plasmids expressing site-directed Rot
154 mutations $F^{10}A/L^{13}A/Q^{14}A/T^{17}A$, $S^{36}A/E^{38}A/E^{39}A$, $Q^{48}A$, $L^{54}A/K^{55}A$, $K^{64}A$-$R^{70}A$, $T^{71}A/N^{74}A$,
155 $R^{91}A$ and $L^{41}A/L^{44}A$ were generated by using a PCR splicing by overlap extension (SOE)
156 approach. Primers are described in Table 5. The mutated PCR products were digested with
157 NdeI and XhoI and then ligated into the *E. coli/S. aureus* shuttle vector pOS1P*lgt*, which had
158 been similarly digested. Point mutants $F^{10}A$, $L^{13}A$, $Q^{14}A$, $Q^{14}E$, $T^{17}A$, $E^{39}A$, $Y^{66}A$, $K^{67}A$, $N^{74}A$
159 and ΔHis were generated by site directed mutagenesis directly on the pOS1P*lgt rot* plasmid
160 via a Quickchange kit (Agilent). The ligation products were then transformed into *E. coli*
161 DH5α. Resulting plasmids were sequenced to confirm desired mutations were present.
162
163 **Construction of an integrated *ssl7* transcriptional reporter *S. aureus* strain.**
164 Integration of the *ssl7* promoter (P*ssl7*) driving enhanced GFP (sGFP) expression into the *S.*
165 *aureus* chromosome was performed by cloning the construct into the suicide plasmid
166 pJC1111, which stably integrates into the SaPI-1 site of *S. aureus* resulting in single copy
167 insertion into the chromosome. Primers are described in Table 5. A PCR amplicon
168 containing P*ssl7* driving sGFP expression was amplified from pOS1sGFP P*ssl7*-*sod*RBS and
169 was subsequently digested and cloned into pJC1111 (24). Integration was initially carried
170 out in RN4220 containing plasmid pRN7203, which encodes the integrase. Phage
171 transduction was employed to generate Newman Wild Type and mutant *rot* strains with
172 the P*ssl7*-sGFP transcriptional reporter integrated into the chromosome.
173
174 **GFP reporter assays.** GFP reporter assays were performed as previously described (24).
175 Briefly, *S. aureus* cultures grown overnight in RPMI/CAS + 10 μg/mL Cm were subcultured

176 1:100 in 5 mL RPMI/CAS + 10 μg/mL Cm and grown at 37°C and 180 rpm. OD_{600} and GFP
177 fluorescence were measured 5 hours post subculture using a Perkin Elmer Envision 2103
178 Multilabel Reader.
179
180 **Immunoblots.** *S. aureus* was grown in RPMI/CAS + 10 μg/mL Cm overnight. These cultures
181 were subcultured 1:100 in 5 mL RPMI/CAS + 10 μg/mL Cm and grown at 37°C and 180
182 rpm. Cells were OD_{600} normalized and pelleted by centrifugation.
183
184 For Hla and Ssl7 immunoblots, exoproteins from culture supernatants were precipitated
185 with 10% trichloroacetic acid (TCA) and incubated at 4°C overnight. Precipitated proteins
186 were sedimented by centrifugation, washed once with 100% ethanol, air-dried,
187 resuspended in SDS-Laemmli buffer, and boiled for 10 minutes. Proteins were resolved on
188 a 12% or 15% SDS-PAGE gel and transferred to nitrocellulose. Membranes were blocked
189 with PBS + 5% milk and probed with either polyclonal rabbit anti-Ssl7 (1:5,000) or
190 polyclonal rabbit anti-Hla (1:1,000). An AlexaFluor680 goat α-rabbit antibody was used at
191 1:25,000 dilution as the secondary antibody. Membranes were imaged using an Odyssey
192 Infrared Imaging System (LI-Cor Biosciences, Lincoln, NE).
193
194 For Rot immunoblots, cell pellets were resuspended in PBS containing 0.1 g 0.1 mm glass
195 beads. Cells were lysed by disruption using a FastPrep-24 Tissue and Cell Homogenizer
196 (MP Biomedicals, Solon, OH) for 40 seconds. Protein concentrations of samples were
197 normalized by bicinchoninic acid (BCA) assay using a BCA Protein Assay Kit (Thermo
198 Scientific). Proteins were resolved on a 4% - 20% gradient SDS-PAGE gel and transferred to

199 nitrocellulose. Membranes were blocked with PBS + 5% milk + 0.1 mg/mL human IgG and
200 probed with polyclonal rabbit anti-Rot primary antibody at 1:1,000 dilution. Secondary
201 antibody and imaging were as described above.
202
203 **RNA isolation.** *S. aureus* cultures grown in RPMI/CAS + 10 μg/mL Cm overnight were
204 diluted to 1:100 in 20 mL RPMI/CAS + 10 μg/mL Cm and grown at 37°C with shaking at
205 180 rpm for 5 hours. Cultures were mixed with an equal volume of 1:1 ethanol:acetone and
206 frozen at -80°C. For RNA extraction, frozen cultures were thawed on ice and cells were
207 pelleted by centrifugation and washed twice with TE. Cells were transferred to MP
208 Biomedicals Lysing Matrix B 2 mL tubes and lysed using the FastPrep-24 Tissue and Cell
209 Homogenizer for 40 seconds (MP Biomedicals, Solon, OH). Cell debris was removed by
210 centrifugation. RNA was isolated from lysates using the RNeasy mini kit (Qiagen, Valencia,
211 CA) according to manufacturer's instructions. On-column DNase digestion was performed
212 using an RNase-free DNase set (Qiagen, Valencia, CA). A second DNase digestion was
213 performed after RNA elution using RQ1 DNaseI (Promega, Madison, WI). RNA was
214 quantified using a nanodrop spectrophotometer and quality was evaluated on an agarose-
215 formaldehyde gel.
216
217 **Quantitative reverse transcriptase PCR (qRT-PCR).** 100 ng purified RNA was used in a
218 SYBER green-based comparative C_T assay (Qiagen, Valencia, CA) in a 7300 Real Time PCR
219 System (Applied Biosystems, Carlsbad, CA) to determine relative quantification of gene
220 transcription from *ssl7*, *spA*, *hla* and *lukE*. 10 ng purified RNA was used to examine
221 amplification of 16S rRNA as an endogenous control. Primers used to detect transcripts are

222 listed in Table 5. Relative quantification of gene expression was determined for duplicate
223 reactions of each strain using the 7300 Real Time Quantitative PCR Software (Applied
224 Biosystems, Carlsbad, CA). Relative gene expression was determined by comparing all
225 strains to an isogenic strain that does not produce Rot or an isogenic strain that produces
226 wild type Rot.
227
228 **Purification of Rot-His from *S. aureus*.** *S. aureus* Newman *rot::spec* strains carrying
229 plasmid pOS1/P*lgt*-Rot-His mutants were grown overnight in TSB + 10 μg/mL Cm, then
230 subcultured 1:100 into 400 mL TSB + 10 μg/mL Cm and grown for 5 hours at 37°C with
231 shaking at 180 rpm. Cells were pelleted by centrifugation at 4,000 rpm for 30 min. and
232 washed once with TSM (50 mM Tris-HCl pH 7.5, 0.5 M sucrose, 10 mM MgCl2). Pellets were
233 resuspended in 20 mL TSM + 25μg/mL lysostaphin. Suspensions were incubated at 37°C
234 for 10 min. Cells were pelleted by centrifugation at 4,000 rpm for 15 min. and washed once
235 with TSM. Pellets were resuspended in 40 mL TBS supplemented with 10 mM imidazole
236 and an EDTA-free protease inhibitor. Cells were lysed by sonication on ice. Soluble proteins
237 were isolated from cellular debris by centrifugation at 20,000 rpm 20 min. at 4°C. Rot was
238 selectively purified by Ni-NTA chromatography and elution with 500 mM imidazole.
239
240 **Electrophoretic Mobility Shift Assay.** The regions upstream of *lukED* and *ssl7* were
241 amplified using biotinylated primers listed in Table 5 to generate DNA probes between 300
242 – 400 base pairs in length. 100 fmol biotinylated probes were mixed with 2 μg Rot-His for a
243 total reaction volume of 20 μL in EMSA buffer (10 mM Tris H-Cl pH 7.4, 50 mM KCl, 5 mM
244 MgCl2, 10% glycerol, 5 μg/mL salmon sperm DNA). Reactions were incubated at room

245 temperature for 20 min. Samples were analyzed on 6% native polyacrylamide gels run at
246 10 mA per gel in Tis-borate EDTA (TBE). Gels were incubated for 15 min. in 50% IPA/5%
247 acetic acid, followed by 15 min. in dH_2O. Gels were developed by incubation for one hour in
248 Streptavidin DyLight (Thermo Scientific, Waltham, MA) diluted 1:1,000 in phosphate
249 buffered saline (PBS) + 0.1% Tween + 5% BSA. Gels were imaged using an Odyssey
250 Infrared Imaging System (LI-Cor Biosciences, Lincoln, NE).
251
252 **Protein structure accession numbers.** The atomic coordinates and structure factors for
253 the Rot structure have been deposited in RCSB Protein Data Bank with accession code
254 4RBR.
255
256 **RESULTS**
257 **X-ray structure determination.** To gain insight into how Rot mediates promoter
258 recognition, we solved a crystal structure of Rot by the Multi-wavelength Anomalous
259 Dispersion (MAD) method using a selenomethionine (SeMet) derivative. The presence of
260 SeMet in the crystal was confirmed by fluorescence spectroscopy, and four selenium sites
261 of each molecule were identified. The resulting experimental phases were used as initial
262 phases in a restrained refinement against the native diffraction data set of 1.7Å resolution.
263 Rot was crystallized in space group P1, with unit cell lengths of 31.6, 37.5, and 63.9 Å and
264 angles of 85.5, 82.3, and 81.3 degrees, and its structure was refined to R_{work} and R_{free} of
265 18.74% and 21.26%, respectively (Table 1). The final model contains residues 6-133 along
266 with 3 additional C-terminal His residues from a Poly-His tag (Fig. 1). A chloride ion,

267 located between the Helix-Turn-Helix (HTH) and the wing and coordinated by backbone
268 amides, was refined into the final model for each monomer (Fig. 1A).
269
270 **Overall structure of the Rot dimer.** The structure shows Rot as a non-crystallographic
271 dimer (Fig. 1A), with two dimers in the asymmetric unit. When superimposed, the two
272 monomers are nearly identical, with inter-chain C_α root-mean-square deviation (RMSD) of
273 0.21 Å (without 3 residues at the tip of the wing that have different conformations between
274 the monomers). The Rot structure is largely helical, with 5 alpha helices (α1-α5) and a
275 single 2-stranded (β1 & β2) beta sheet for each monomer (Fig. 1B). It is composed of 3
276 distinct structural regions (Fig. 1B & C): the HTH motif, the wing, and the dimerization
277 helices. The HTH motif is composed of two helices (α3 and α4) connected by a short loop.
278 The C-terminal portion of this motif is termed the Recognition Helix (RH, α4), and is likely
279 to make specific contacts with the backbone and bases of the major groove of DNA (28-30).
280 The wing region of Rot consists of the two β-strands (β1 & β2), connected by an 11-residue
281 flexible loop with a high crystallographic B-factor and slightly different conformations at
282 the loop tips (Fig. 1D). The two long helices, N-terminal α1 and C-terminal α5, as well as
283 helix α2 located below the HTH motif from each monomer, join together to form a head-to-
284 head dimer with 2-fold symmetry about a vertical axis at the center of the dimer. The long
285 α1 and α5 from each monomer come together to form a 4-helix bundle, creating an
286 extensive hydrophobic interface between the monomers with a buried surface area of
287 ~1800 $Å^2$ (Fig. 2A). There are also hydrogen bonds and water-mediated interactions
288 between the monomers (Fig. 2B), including the formation of a water-mediated hydrogen
289 bond network between side chain of E^{16} of one monomer and the side chains of R^{37} of the

290 other monomer (Fig. 2C), and hydrogen bonds between the side chains of the symmetry-
291 related Q^{124} from each monomer (Fig. 2D).
292
293 The Rot dimer has a highly negatively charged surface (Fig. 3A), consistent with its acidic pI
294 of 5.1, which is 2 pH units below that of any other SarA family member and more than 3 pH
295 units below the family average pI of 8.2. There are 21 negatively and 17 positively charged
296 residues per monomer, with 2 N-terminal lysine residues not observed in the crystal
297 structure. The majority of the positively charged residues are located in the WHTH domain,
298 rendering it overall positively charged, consistent with its DNA binding function. The
299 dimerization helices are negatively charged; they, together with the positively charged
300 WHTH domains, create an asymmetric charge distribution that would help to orient the
301 WHTH domains in the Rot dimer toward the negatively charged phosphate backbone of the
302 target DNA. A comparison of Rot's structure to those of other SarA family members and
303 WHTH-containing proteins showed a correlation between sequence conservation and
304 charge distributions. Sequence conservation mapping indicates this group of proteins to be
305 most conserved in the WHTH region and least conserved in the dimerization helices on the
306 underside of the dimer (Table 2, Fig. 3B & C). Interestingly, among the SarA family and
307 other WHTH proteins, the electrostatic profile mimics the conservation profile, i.e., the
308 surface of conserved residue regions are also positively charged, and vice versa (Fig. 3A &
309 C).
310
311 **Structural implication of Rot's DNA binding.** To understand how Rot interacts with DNA,
312 we superimposed its structure with that of other WHTH proteins in complex with DNA, and

313 found that the Rot dimer is structurally highly homologous to the *Bacillus subtilis* OhrR
314 protein (PDB ID 1Z9C) (43), with a RMSD of ~2.0Å when the WHTH domains are
315 superimposed (Table 2). Like Rot, OhrR forms a dimer using both N-terminal and C-
316 terminal helices, although its C-terminal dimerization domain is formed by two helices (α5
317 and α6), while Rot has a relatively straight long single helix (α5). By superimposing the
318 WHTH domain of Rot onto that of OhrR in the DNA complex, we were able to predict the
319 residues that potentially interact with the DNA (Fig. 4A & B).
320
321 Residues that predicted from our modeling to interact with DNA can be divided into two
322 groups: those that likely make sequence-specific contact with the bases of DNA (colored
323 orange in Fig. 1B) or those that likely make non-specific contact with the backbone of DNA
324 (purple in Fig. 1B). Seven residues (^{64}KPYKRTR^{70}) located at the N-terminal corner of the
325 RH are predicted to bind into the major groove of DNA (Fig. 4A & B); thus, they can
326 potentially make sequence specific interactions. Residue R^{91}, located at the tip of the wing,
327 is predicted to insert its side chain into the minor groove of DNA; thus it can also interact
328 with DNA in a sequence specific fashion. Thirteen residues from different Rot domains are
329 predicted to be involved in non-specific DNA interactions, forming contacts with the DNA
330 backbones. When we fit the Rot structure onto that of OhrR-DNA complex, the position of
331 the chloride ion in each monomer overlapped with that of a phosphate of the DNA
332 backbone; thus, the chloride ion will likely be displaced upon DNA binding (Fig. 1A and 4A).
333
334 Rot's structure was also analyzed using the Optimal Docking Area (ODA) tool of ICM to
335 predict potential sites of protein-partner interaction (44). ODA applies an algorithm

336 benchmarked to accurately predict protein-interaction regions based on the biophysical
337 properties of the functional groups on the surface of the protein. The residues predicted by
338 ODA to interact with protein partners are located on the undersurface of Rot at the junction
339 between the two monomers, including F^{10}, L^{13}, Q^{14}, and T^{17} from helix α1 of one monomer
340 and Q^{48} of helix α2 from the other monomer (Fig. 4C and D).
341
342 **Functional Studies of Specific Rot Residues.** Based on the predicted DNA and protein
343 partner binding regions in our model, we made 4 sets of alanine substitutions to further
344 map the functionally important residues (Table 3, Fig. 5A - E). The first set of mutants
345 included substitutions in the WHTH domain that may affect specific binding between Rot
346 and DNA: group substitutions of residues K^{64}-R^{70} that line the top of the RH and individual
347 substitutions of Y^{66} and K^{67} of RH and R^{91} of the wing (Fig. 5B and C). The second set of
348 mutants included substitutions in the WHTH domain that were predicted to affect non-
349 specific binding of DNA: group substitutions of L^{54} and K^{55} of α3 (Fig. 5B), and of T^{71} and
350 N^{74} on the underside of the recognition helix (α4), as well as the individual substitution of
351 N^{74} (Fig. 5C). The third set of mutants included substitutions in the core helices to perturb
352 non-specific interactions with DNA: group substitutions of L^{41} and L^{44} in addition to S^{37}, E^{38}
353 and E^{39} of α2, and the individual substitution of E^{39} (Fig. 5C and D). The fourth set of
354 mutants included substitutions of surface residues of Rot that are predicted to make
355 contact with potential protein partners: group substitutions of F^{10}, L^{13}, Q^{14}, and T^{17} and
356 individual substitutions of F^{10}, L^{13}, Q^{14}, T^{17} and Q^{48} (Fig. 5E). We also made a specific
357 substitution of Q^{14} to glutamic acid to determine if we could alter the specificity of this
358 interface.

359

360 Mutant constructs were cloned into the vector pOS1P*lgt* (45). Immunoblot analysis was
361 performed to ensure that mutation of these residues did not impact Rot production (data
362 not shown). We then tested these mutants for activation of the *ssl7* promoter (24, 31).
363 Promoter activation function was quantified by the use of a single copy integrated P*ssl7*-
364 sGFP transcriptional reporter (Fig. 6A). Although a number of mutations, including $F^{10}A$,
365 $L^{13}A$, $Q^{14}A/E$, $T^{17}A$, $E^{39}A$, $L^{41}A$ and $L^{44}A$, $Q^{48}A$, $K^{67}A$, $N^{74}A$, did not result in significant
366 changes in promoter activation compared to WT Rot, six of the tested mutations, with
367 alanine substitutions of either individual or group residues, resulted in drastic changes in
368 function from WT Rot (Fig. 6A). The phenotypes observed with the transcriptional
369 reporters were further validated by monitoring the levels of the Ssl7 protein in culture
370 filtrates (Fig. 6B).

371

372 **Rot differentially activates and represses target genes.** Quantitative reverse-
373 transcription PCR (qRT-PCR) was used to further assess the ability of Rot and the Rot
374 mutants described in Fig. 6 to either activate transcription of *ssL7* and *spa* (Fig. 7A & B) (20,
375 24, 31, 46), or repress transcription of *lukE* and *hla* (Fig. 7C & D) (19, 23, 47). Comparison
376 of activation and repression of these genes revealed that R^{91}, in the wing motif, and L^{54}/K^{55},
377 in the RH α3, are the most important residues for Rot-mediated regulation of both
378 repressed and activated genes. The $F^{10}A/L^{13}A/Q^{14}A/T^{17}A$ mutant demonstrated
379 intermediate effects on both activation and repression activity of the tested targets.
380 Interestingly, the remaining mutants demonstrated effects on Rot activity that varied
381 among the studied promoters. For example, the $Y^{66}A$ mutant had an intermediate effect on

382 activation of *ssl7* and repression of *hla*, but severely impaired activation of *spa*, while
383 having almost no effect on repression of *lukED*. The $T^{71}A/N^{74}A$ mutant demonstrated
384 intermediate effects on activity of all promoters except *lukED*, where it had no effect on
385 repression of this gene. Finally, the $S^{36}A/E^{38}A/E^{39}A$ mutant had little effect on activation of
386 *spa* or repression of *lukED*, but significantly decreased the ability of Rot to activate *ssl7* and
387 repress *hla*. Taken together, these results indicate that certain residues may be of more
388 importance in the recognition of specific promoters, highlighting a potential novel
389 mechanism by which Rot differentiates target promoters.
390
391 To determine whether substitution of these residues altered the ability of Rot to directly
392 bind these target promoters, electromobility shift assays (EMSAs) were performed. In
393 correlation with the qRT-PCR results, Rot $L^{54}A/K^{55}A$ and $R^{91}A$ no longer bind to the *ssl7*
394 promoter, correlating with a loss of activation (Fig. 7E). Additionally, Rot $L^{54}A/K^{55}A$ and
395 $R^{91}A$ no longer bind to the *lukED* promoter, corroborating the qRT-PCR data, which
396 demonstrates a loss of repression of *lukED* by these mutants (Fig. 7F). These results
397 suggest that loss of activation or repression of these promoters is due to lack of binding to
398 the target promoters. Interestingly, the Rot $F^{10}A/L^{13}A/Q^{14}A/T^{17}A$ and $Y^{66}A$ mutants still
399 appear to retain some binding ability, which may account for the intermediate
400 activation/repression phenotypes observed by qRT-PCR (Fig. 7E & F).
401
402 The large effects on Rot function and DNA binding resulting from mutants of R^{91} on the
403 wing and L^{54}/K^{55} adjacent to the wing suggest that these two sites likely play an important
404 role in the insertion of the wing into the minor groove of DNA (Figs. 6A and 7). The alanine

405 substitution of residue Y^{66} at the very tip of the RH (thus likely bind the bases in the major
406 groove) had a much larger effect on Rot's function than that of the neighboring residue K^{67}
407 (Fig. 6B), but this Y^{66} mutation did not have a strong effect on promoter binding (Fig. 7E &
408 F), suggesting an alternative role for Y^{66} in Rot activity. Interestingly, Y^{66} and the other
409 mutated residues of the HTH and helical core have a less pronounced and more varied
410 effect on activating or repressing transcription than residues involved with insertion of the
411 wing into the minor groove. These results may suggest that interactions between the wing
412 and minor groove are important for Rot binding to DNA, while residues in the HTH and
413 helical core facilitate recognition and differentiation among target promoters.
414

415 **DISCUSSION**

416 Rot is a central regulator of *S. aureus* virulence and is known to specifically interact with
417 target promoters (19, 20, 22-25, 47). Work presented here aimed to gain insight into how
418 Rot interacts with promoters by solving a high-resolution crystal structure. The structure
419 of Rot showed a conserved DNA-binding face that is positively charged despite the overall
420 very acidic pI of the protein. Like some other WHTH proteins that bind DNA (such as
421 OhrR), Rot's electrostatic profile is asymmetrical and can therefore orient the WHTH motif
422 toward the DNA helix. This specific electrostatic profile and a delicate charge balance may
423 have profound functional significance. One possibility is that the overall negative charge of
424 Rot may create a slight repulsion between Rot and the DNA, and this repulsion can be
425 altered by interactions with protein partners that possess an overall positive charge, such
426 as RNA polymerase. Therefore, Rot's unique electrostatic features may serve a functional
427 purpose enabling its central role in regulating the *S. aureus* virulon.

428

429 Despite Rot's known ability to interact specifically with certain promoters (20, 22, 24, 25),
430 the binding site of Rot is still unknown. Our structure allows several predictions about its
431 potential DNA binding mechanism. First, the Rot dimer is highly symmetric with an almost
432 exact twofold rotational symmetry, suggesting that the DNA sequences in the Rot-
433 interacting promoters will likely contain palindromic elements. Second, the distance in the
434 dimer between the Cα atoms of the two R^{91} residues, whose side chains likely penetrate
435 into the minor groove of DNA, is 60 Å (Fig. 5A). Given that the length per base pair of a
436 standard DNA helix is 3.3 Å (48), Rot likely interacts with a section of DNA about 18 base
437 pairs long. This is in agreement with a study by Rechtin and colleagues, who made a similar
438 prediction about SarA (49); however, the SarA binding site is still a subject of debate (50,
439 51). It should be noted that this estimation of the Rot binding site length is rudimentary, as
440 the wing regions are very flexible and the distance between the R^{91} residues can vary.
441 Third, the side chain of R^{91}, which is part of the conserved DER region of SarA family
442 proteins, will interact specifically with a base in the minor groove. The crystal structure of
443 OhrR-DNA showed that the side chain of the corresponding arginine forms a base-specific
444 interaction with the oxygen atom of a thymine. Since it is highly conserved in the SarA
445 family (Fig. 3B), R^{91} will likely also interact with a thymine in the Rot-interacting
446 promoters. In addition, K^{55}, adjacent to the wing, is also highly conserved among SarA
447 family proteins (Fig. 3B), suggesting this residue may play a key role in interaction with
448 DNA as well. These predictions are consistent with our functional data demonstrating that
449 alanine substitution of R^{91} and the two residues L^{54} and K^{55} had more substantial effects on
450 activation or repression of promoters than other mutated residues of the HTH or the

451 helices at the center of the dimer. The loss of either activation or repression that results
452 from substitution of R^{91} and L^{54}/K^{55}, combined with the conservation of the DER region in
453 the SarA family, implies a uniform mechanism utilized by this protein family for the
454 interaction of the wing region with the minor groove.
455
456 In contrast, mutations of the HTH region of Rot have a much more varied effect on the
457 activation or repression of promoters (Fig. 7). It is possible that the determinants of
458 functional selectivity between different Rot-interacting promoters may reside in the
459 residues of the RH, which likely make contact with the major groove of DNA. For example,
460 residue Y^{66}, projecting from the top of the RH, could play the role of selectivity filter for
461 different promoters; this residue is unique to Rot and its substitution to alanine has a
462 differential effect on activation versus repression. The residues on the top of the
463 recognition helix of other SarA family members are variable and likely play a similar role,
464 such as P^{71}, K^{74}, and/or R^{75} of MgrA; S^{65} of SarS; Y^{63} of SarR; P^{65} and/or K^{69} of SarA; and S^{68}
465 and/or T^{70} of OhrR (Fig. 3B).
466
467 While we writing the present study, Zhu *et al* published a structure of Rot of equal
468 resolution to ours, that agrees completely with the findings described herein (e.g. Rot is a
469 homodimer and has a winged HTH DNA binding domain) (52). In our Rot structure,
470 however, we were able to capture the wing domain, which was absent in the Zhu *et al*
471 structure (52), providing a more detailed molecular picture of Rot. The mutagenesis
472 studies described in our study also validate and extend the Zhu *et al* findings, highlighting
473 the role of critical residues for Rot function. In addition, while Zhu *et al* discussed the

474 potential contribution of residues involved in the hydrophobic dimer interface, we actually
475 tested residues within this interface and showed that they contribute to Rot function,
476 which is consistent with the finding by Zhu *et al* that demonstrates that the formation of
477 the Rot dimer is required for Rot binding to synthetic DNA. One of the most important
478 differences between our study and that of Zhu *et al* is the fact that Zhu *et al* performed Rot
479 binding studies exclusively with a synthetic AT rich DNA, while our studies were done
480 using DNA from Rot-regulated promoters. Moreover, our study provided greater insight
481 into how Rot regulates target promoters by analyzing four different promoters in total –
482 two repressed and two activated. By analyzing these promoters, we discovered that certain
483 mutations exhibit promoter-dependent effects, thus highlighting the fact that Rot interacts
484 with target promoters differently. Altogether, the data presented herein provide insight
485 into the structure and function of Rot as a transcriptional activator and repressor.
486 However, it is clear that additional work needs to be undertaken to better understand Rot's
487 selectivity for activated versus repressed promoters, as well as to identify a specific Rot
488 binding site.
489

490 **ACKNOWLEGEMENTS**

491 We would like to thank Dr. John Fraser for providing the anti-Ssl7 antibody and Dr.
492 Alexander Horswill for providing the sGFP plasmid. Research reported in this publication
493 was supported in part by funds of a Graduate Research Fellowship to A.K. from the National
494 Science and Engineering Research Council of Canada and by the National Institute Of
495 Allergy And Infectious Diseases of the National Institutes of Health under Award Number
496 R21AI101533 to V.J.T. The content is solely the responsibility of the authors and does not

497 necessarily represent the official views of the National Institutes of Health

498

499 **REFERENCES**

500 1. **Lowy FD.** 1998. *Staphylococcus aureus* infections. The New England Journal of
501 Medicine **339:**520-532.

502 2. **Diekema DJ, Pfaller MA, Schmitz FJ, Smayevsky J, Bell J, Jones RN, Beach M,**
503 **Group SP.** 2001. Survey of infections due to Staphylococcus species: frequency of
504 occurrence and antimicrobial susceptibility of isolates collected in the United States,
505 Canada, Latin America, Europe, and the Western Pacific region for the SENTRY
506 Antimicrobial Surveillance Program, 1997-1999. Clin Infect Dis **32 Suppl 2:**S114-
507 132.

508 3. **Jones RN.** 2003. Global epidemiology of antimicrobial resistance among
509 community-acquired and nosocomial pathogens: a five-year summary from the
510 SENTRY Antimicrobial Surveillance Program (1997-2001). Seminars in respiratory
511 and critical care medicine **24:**121-134.

512 4. **Fridkin SK, Hageman JC, Morrison M, Sanza LT, Como-Sabetti K, Jernigan JA,**
513 **Harriman K, Harrison LH, Lynfield R, Farley MM.** 2005. Methicillin-resistant
514 *Staphylococcus aureus* disease in three communities. The New England Journal of
515 Medicine **352:**1436-1444.

516 5. **Deleo FR, Otto M, Kreiswirth BN, Chambers HF.** 2010. Community-associated
517 meticillin-resistant *Staphylococcus aureus*. Lancet **375:**1557-1568.

518 6. **Klevens R, Morrison M, Nadle J, Petit... S.** 2007. Invasive methicillin-resistant
519 *Staphylococcus aureus* infections in the United States. The Journal of the American
520 Medical Association.
521 7. **Hiramatsu K, Aritaka N, Hanaki H, Kawasaki S, Hosoda Y, Hori S, Fukuchi Y,**
522 **Kobayashi I.** 1997. Dissemination in Japanese hospitals of strains of *Staphylococcus*
523 *aureus* heterogeneously resistant to vancomycin. Lancet **350:**1670-1673.
524 8. **Waters CM, Bassler BL.** 2005. Quorum sensing: cell-to-cell communication in
525 bacteria. Annual review of cell and developmental biology **21:**319-346.
526 9. **Novick RP, Geisinger E.** 2008. Quorum sensing in staphylococci. Annu Rev Genet
527 **42:**541-564.
528 10. **Recsei P, Kreiswirth B, O'Reilly M, Schlievert P, Gruss A, Novick RP.** 1986.
529 Regulation of exoprotein gene expression in *Staphylococcus aureus* by agar. Mol Gen
530 Genet **202:**58-61.
531 11. **Queck SY, Jameson-Lee M, Villaruz AE, Bach TH, Khan BA, Sturdevant DE,**
532 **Ricklefs SM, Li M, Otto M.** 2008. RNAIII-independent target gene control by the agr
533 quorum-sensing system: insight into the evolution of virulence regulation in
534 *Staphylococcus aureus*. Molecular Cell **32:**150-158.
535 12. **Janzon L, Lofdahl S, Arvidson S.** 1989. Identification and nucleotide sequence of
536 the delta-lysin gene, hld, adjacent to the accessory gene regulator (agr) of
537 *Staphylococcus aureus*. Mol Gen Genet **219:**480-485.
538 13. **Novick RP, Ross HF, Projan SJ, Kornblum J, Kreiswirth B, Moghazeh S.** 1993.
539 Synthesis of staphylococcal virulence factors is controlled by a regulatory RNA
540 molecule. Embo J **12:**3967-3975.

541 14. **Benito Y, Kolb FA, Romby P, Lina G, Etienne J, Vandenesch F.** 2000. Probing the
542 structure of RNAIII, the *Staphylococcus aureus* agr regulatory RNA, and
543 identification of the RNA domain involved in repression of protein A expression.
544 RNA **6:**668-679.
545 15. **Boisset S, Geissmann T, Huntzinger E, Fechter P, Bendridi N, Possedko M,**
546 **Chevalier C, Helfer AC, Benito Y, Jacquier A, Gaspin C, Vandenesch F, Romby P.**
547 2007. *Staphylococcus aureus* RNAIII coordinately represses the synthesis of
548 virulence factors and the transcription regulator Rot by an antisense mechanism.
549 Genes & Development **21:**1353-1366.
550 16. **Geisinger E, Adhikari RP, Jin R, Ross HF, Novick RP.** 2006. Inhibition of rot
551 translation by RNAIII, a key feature of agr function. Mol Microbiol **61:**1038-1048.
552 17. **Huntzinger E, Boisset S, Saveanu C, Benito Y, Geissmann T, Namane A, Lina G,**
553 **Etienne J, Ehresmann B, Ehresmann C, Jacquier A, Vandenesch F, Romby P.**
554 2005. *Staphylococcus aureus* RNAIII and the endoribonuclease III coordinately
555 regulate spa gene expression. EMBO J **24:**824-835.
556 18. **Morfeldt E, Taylor D, von Gabain A, Arvidson S.** 1995. Activation of alpha-toxin
557 translation in *Staphylococcus aureus* by the trans-encoded antisense RNA, RNAIII.
558 EMBO J **14:**4569-4577.
559 19. **McNamara PJ, Milligan-Monroe KC, Khalili S, Proctor RA.** 2000. Identification,
560 Cloning, and Initial Characterization of *rot*, a Locus Encoding a Regulator of
561 Virulence Factor Expression in *Staphylococcus aureus*. J Bacteriol **182:**3197-3203.

562 20. **Said-Salim B, Dunman PM, McAleese FM, Macapagal D, Murphy E, McNamara**
563 **PJ, Arvidson S, Foster TJ, Projan SJ, Kreiswirth BN.** 2003. Global Regulation of
564 *Staphylococcus aureus* Genes by Rot. J Bacteriol **185:**610-619.
565 21. **Novick RP.** 2003. Autoinduction and signal transduction in the regulation of
566 staphylococcal virulence. Mol Microbiol **48:**1429-1449.
567 22. **McNamara PJ, Bayer AS.** 2005. A rot mutation restores parental virulence to an
568 agr-null *Staphylococcus aureus* strain in a rabbit model of endocarditis. Infect
569 Immun **73:**3806-3809.
570 23. **Alonzo F, 3rd, Benson MA, Chen J, Novick RP, Shopsin B, Torres VJ.** 2012.
571 *Staphylococcus aureus* leucocidin ED contributes to systemic infection by targeting
572 neutrophils and promoting bacterial growth in vivo. Mol Microbiol **83:**423-435.
573 24. **Benson MA, Lilo S, Wasserman GA, Thoendel M, Smith A, Horswill AR, Fraser J,**
574 **Novick RP, Shopsin B, Torres VJ.** 2011. *Staphylococcus aureus* regulates the
575 expression and production of the staphylococcal superantigen-like secreted
576 proteins in a Rot-dependent manner. Mol Microbiol **81:**659-675.
577 25. **Tseng CW, Stewart GC.** 2005. Rot repression of enterotoxin B expression in
578 *Staphylococcus aureus*. J Bacteriol **187:**5301-5309.
579 26. **Cheung AL, Bayer AS, Zhang G, Gresham H, Xiong YQ.** 2004. Regulation of
580 virulence determinants in vitro and in vivo in *Staphylococcus aureus*. FEMS Immunol
581 Med Microbiol **40:**1-9.
582 27. **Brennan RG.** 1993. The winged-helix DNA-binding motif: another helix-turn-helix
583 takeoff. Cell **74:**773-776.

584 28. **Ohlendorf DH, Anderson WF, Fisher RG, Takeda Y, Matthews BW.** 1982. The
585 molecular basis of DNA-protein recognition inferred from the structure of cro
586 repressor. Nature **298:**718-723.
587 29. **Ohlendorf DH, Anderson WF, Matthews BW.** 1983. Many gene-regulatory
588 proteins appear to have a similar alpha-helical fold that binds DNA and evolved
589 from a common precursor. Journal of Molecular Evolution **19:**109-114.
590 30. **Sauer RT, Yocum RR, Doolittle RF, Lewis M, Pabo CO.** 1982. Homology among
591 DNA-binding proteins suggests use of a conserved super-secondary structure.
592 Nature **298:**447-451.
593 31. **Benson MA, Lilo S, Nygaard T, Voyich JM, Torres VJ.** 2012. Rot and SaeRS
594 cooperate to activate expression of the staphylococcal superantigen-like
595 exoproteins. J Bacteriol **194:**4355-4365.
596 32. **Read RJ, Sussman JL.** 2007. Evolving Methods for Macromolecular Crystallography,
597 vol. 245. Springer.
598 33. **Winn MD, Ballard CC, Cowtan KD, Dodson EJ, Emsley P, Evans PR, Keegan RM,**
599 **Krissinel EB, Leslie AG, McCoy A, McNicholas SJ, Murshudov GN, Pannu NS,**
600 **Potterton EA, Powell HR, Read RJ, Vagin A, Wilson KS.** 2011. Overview of the
601 CCP4 suite and current developments. Acta Crystallogr D Biol Crystallogr **67:**235-
602 242.
603 34. **Project CC.** 1994. The CCP4 suite: programs for protein crystallography, p. 760-763,
604 Acta Crystallogr D Biol Crystallogr, 1994/09/01 ed, vol. 50.
605 35. **Sheldrick GM.** 2010. Experimental phasing with SHELXC/D/E: combining chain
606 tracing with density modification. Acta Crystallogr D Biol Crystallogr **66:**479-485.

607 36. **Cowtan K.** 2006. The Buccaneer software for automated model building. 1. Tracing
608 protein chains. Acta Crystallogr D Biol Crystallogr **62:**1002-1011.
609 37. **Emsley P, Lohkamp B, Scott WG, Cowtan K.** 2010. Features and development of
610 Coot. Acta Crystallogr D Biol Crystallogr **66:**486-501.
611 38. **Murshudov GN, Skubak P, Lebedev AA, Pannu NS, Steiner RA, Nicholls RA,**
612 **Winn MD, Long F, Vagin AA.** 2011. REFMAC5 for the refinement of macromolecular
613 crystal structures. Acta Crystallogr D Biol Crystallogr **67:**355-367.
614 39. **Adams PD, Afonine PV, Bunkoczi G, Chen VB, Davis IW, Echols N, Headd JJ,**
615 **Hung LW, Kapral GJ, Grosse-Kunstleve RW, McCoy AJ, Moriarty NW, Oeffner R,**
616 **Read RJ, Richardson DC, Richardson JS, Terwilliger TC, Zwart PH.** 2010.
617 PHENIX: a comprehensive Python-based system for macromolecular structure
618 solution. Acta Crystallogr D Biol Crystallogr **66:**213-221.
619 40. **Schrodinger, LLC.** 2010. The PyMOL Molecular Graphics System, Version 1.3r1.
620 41. **Abagyan R, Totrov M, Kuznetsov D.** 1994. ICM—A new method for protein
621 modeling and design: Applications to docking and structure prediction from the
622 distorted native conformation. Journal of Computational Chemistry **15:**488-506.
623 42. **Krissinel E, Henrick K.** 2007. Inference of macromolecular assemblies from
624 crystalline state. J Mol Biol **372:**774-797.
625 43. **Hong M, Fuangthong M, Helmann JD, Brennan RG.** 2005. Structure of an OhrR-
626 ohrA operator complex reveals the DNA binding mechanism of the MarR family.
627 Molecular Cell **20:**131-141.
628 44. **Fernandez-Recio J, Totrov M, Abagyan R.** 2002. Soft protein-protein docking in
629 internal coordinates. Protein Sci **11:**280-291.

630 45. **Bubeck Wardenburg J, Williams WA, Missiakas D.** 2006. Host defenses against
631 *Staphylococcus aureus* infection require recognition of bacterial lipoproteins. Proc
632 Natl Acad Sci U S A **103:**13831-13836.
633 46. **Gao J, Stewart GC.** 2004. Regulatory elements of the *Staphylococcus aureus* protein
634 A (Spa) promoter. J Bacteriol **186:**3738-3748.
635 47. **Benson MA, Ohneck EA, Ryan C, Alonzo F, 3rd, Smith H, Narechania A,**
636 **Kolokotronis SO, Satola SW, Uhlemann AC, Sebra R, Deikus G, Shopsin B, Planet**
637 **PJ, Torres VJ.** 2014. Evolution of hypervirulence by a MRSA clone through
638 acquisition of a transposable element. Mol Microbiol **93:**664-681.
639 48. **Sinden RR.** 1994. DNA structure and function 1st ed ed. Academic Press.
640 49. **Rechtin TM, Gillaspy AF, Schumacher MA, Brennan RG, Smeltzer MS, Hurlburt**
641 **BK.** 1999. Characterization of the SarA virulence gene regulator of *Staphylococcus*
642 *aureus*. Mol Microbiol **33:**307-316.
643 50. **Chien Y, Manna AC, Projan SJ, Cheung AL.** 1999. SarA, a global regulator of
644 virulence determinants in *Staphylococcus aureus*, binds to a conserved motif
645 essential for sar-dependent gene regulation. J Biol Chem **274:**37169-37176.
646 51. **Sterba KM, Mackintosh SG, Blevins JS, Hurlburt BK, Smeltzer MS.** 2003.
647 Characterization of *Staphylococcus aureus* SarA binding sites. J Bacteriol **185:**4410-
648 4417.
649 52. **Zhu Y, Fan X, Zhang X, Jiang X, Niu L, Teng M, Li X.** 2014. Structure of Rot, a global
650 regulator of virulence genes in *Staphylococcus aureus*. Acta Crystallogr D Biol
651 Crystallogr **70:**2467-2476.
652

653 **Table 1.** Data collection and refinement statistics. Data collection statistics are shown for the native data set and those used
654 for MAD phasing (peak, inflection, remote). The final model was refined against the native set.
655

	Native	Selenomethionine Derivative		
		Peak	Remote	Inflection
Data collection				
Wavelength (Å)	1.0	0.9793	0.913	0.9797
Space group	P1	P1	P1	P1
Cell dimensions				
a, b, c	31.56, 37.53, 63.91	31.70, 38.13, 64.08	31.73, 38.22, 64.13	31.71, 38.17, 64.19
alpha, beta, gamma	85.45, 82.26, 81.26	85.60, 82.06, 81.54	85.64, 82.10, 81.28	85.56, 82.06, 81.45
Resolution Range (Å)	37.03-1.7 (1.79-1.7)[a]	37.65-1.86 (1.96-1.86)[a]	37.72-1.73 (1.82-1.73)[a]	37.68-1.86 (1.96-1.86)[a]
Total reflections	113354 (15961)	92762 (13115)	114487 (16212)	93035 (13094)
Unique reflections	29564 (4221)	23720 (3384)	29331 (4195)	23733 (3384)
Rsym (%)	0.074 (0.424)	0.081 (0.617)	0.092 (0.858)	0.070 (0.645)
Mean I/sigma(I)	10.8 (2.8)	9.4 (1.7)	7.6 (0.8)	10.8 (1.6)
Multiplicity	3.8 (3.8)	3.9 (3.9)	3.9 (3.9)	3.9 (3.9)
Completeness (%)	93.7 (91.7)	95.6 (93.5)	95.4 (93.3)	95.3 (93.1)
Refinement				
Resolution (Å)	31.6 Å/1.7 Å			
R-factor	0.19 (0.27)			
R-free	0.21 (0.32)			
No. of atoms	2589			
Macromolecules				
Protein	2168			
Ligand/ion	2			
Water	419			
Protein Residues	262			
B-factors	29.7			
Protein	28.1			
Solvent	37.8			
rmsd				

Bond lengths (Å)	0.006
Bond angles (°)	0.879
Ramachandran favored (%)	98.6
Ramachandran outliers (%)	0.39
Clashscore	5.57

656 [a] Values in parentheses are stated for the highest resolution bin for each structure.

657

658 **Table 2.** Sequence and structural comparison of Rot to SarA and WHTH proteins. Rot's sequence and structure are compared
659 to other SarA family members and several WHTH-containing proteins whose structures were solved in complex with DNA.
660 Tabulated data shown with respect to Rot are: the PDB ID of each structure; the sequence identity of the entire protein; the
661 sequence identity of the WHTH region defined by structural alignment; the root-mean-square devition (RMSD) of the
662 monomer (in the case of 1P4X, only have the protein which corresponds to one Rot monomer was compared); the RMSD of the
663 WHTH region defined by structural alignment; the isoelectric point of each protein defined by the whole protein sequence.
664
665

Protein	PDB ID	Identity (%)	Identity WHTH (%)	RMSD (Å)	RMSD WHTH (Å)	PI
Rot	-	-	-	-	-	5.1
SarA family members						
SarA	2FNP	19	26	4.6	2.4	7.8
SarR	1HSJ	22	40	6.3	1.7	9.3
SarS	1P4X	19	21	5.5	2.3	8.9
MgrA	2BV6	14	17	5.6	1.9	7.0
DNA complexes						
OhrR	1Z9C	13	24	3.7	2.1	6.3
SlyA	3Q5F	8.3	14	6.1	2.3	6.2
MecI	1SAX	5.7	7.3	7.2	2.4	8.9
IscR	4HF1	2.3	7.5	5.7	2.7	6.8
RTP	1F4K	4.1	11.9	7.2	3.7	9.5

666
667

668 **Table 3.** Site-direction mutations in Rot. The location of each mutation within the protein
669 and the predicted contact interrupted by each mutant is indicated.
670

Mutation	Location	Predicted Contact
$R^{91}A$	Wing	Specific DNA
$K^{64}A$ – $R^{70}A$	HTH-RH	Specific DNA
$Y^{66}A$	HTH-RH	Specific DNA
K67A	HTH-RH	Specific DNA
$L^{54}A/K^{55}A$	HTH-α3	Non-specific DNA
$T^{71}A/N^{74}A$	HTH-RH	Non-specific DNA
$N^{74}A$	HTH-RH	Non-specific DNA
$L^{41}A/L^{44}A$	Core-α2	Non-specific DNA
$S^{36}A/E^{38}A/E^{39}A$	Core-α2	Non-specific DNA
$E^{39}A$	Core-α2	Non-specific DNA
$F^{10}A/L^{13}A/Q^{14}A/T^{17}A$	Core-α1	Protein Partners
$F^{10}A$	Core-α1	Protein Partners
$L^{13}A$	Core-α1	Protein Partners
$Q^{14}A$	Core-α1	Protein Partners
$Q^{14}E$	Core-α1	Protein Partners
$T^{17}A$	Core-α1	Protein Partners
$Q^{48}A$	Core-α2	Protein Partners

671

672 **Table 4.** Bacterial strains used in this study.
673

Strain	Background	Description	Genotype	Reference
RN4220	8325-4	Restriction deficient cloning host		Kreiswirth et al 1962
RN9011	RN4220	RN4220 containing the pRN7023 vector encoding the SaPI integrase		Geisinger et al., 2008
VJT 1.01	Newman	Wild type	wildtype	Duthie and Lorenz 1952
VJT 34.79	VJT 1.01	Newman wildtype containing the *ssl7* promoter driving *gfp* expression integrated into the chromosome	wildtype	This study
VJT 9.98	VJT 1.01	Transduction of *rot::Tn917* from RN10623 into VJT 1.01	*rot::Tn917*	Benson et al 2011
VJT 34.84	VJT 9.98	Newman *rot::Tn917* containing the *ssl7* promoter driving *gfp* expression integrated into the chromosome	*rot::Tn917*	This study

674

675 **Table 5.** Primers used in this study.
676

#	Name	Sequence	Description
341	pssl7-F-PstI	5'-CCCC-CTGCAG-GCAGACTAGTAATTGTAGGG	P*ssl7-sgfp* reporter
489	sGFP-R-BamHI	5'-CCC-GGATCC-TTAGTGGTGGTGGTGGTGG	P*ssl7-sgfp* reporter
1118	Rot-Mut1-F-NdeI	5'-CCCCCATATGATGAAAAAAGTAAATAACGACACTG TAGCAGGAATTGCAGCATTAGAAGCACTTTTGG	Forward primer to make a Rot $F^{10}A/L^{13}A/Q^{14}A/T^{17}A$ mutant. Use with primer 311 to clone into pOS1P*lgt*
1120	Rot-Mut3-F	5'-CAAAATGGCAAGAGCAGCAATTTTAATTTTACTAAC	Forward SOEing primer to make a Rot $S^{36}A/E^{38}A/E^{39}A$ mutant. Use with primer 311.
1121	Rot-Mut3-R	5'-GTTAGTAAAATTAAAATTGCTGCTCTTGCCATTTTG	Reverse SOEing primer to make a Rot $S^{36}A/E^{38}A/E^{39}A$ mutant. Use with primer 313.
1122	Rot-Mut4-F	5'-CTTTATGGGCAAAAGGTTCTATGAC	Forward SOEing primer to make a Rot $Q^{48}A$ mutant. Use with primer 311.
1123	Rot-Mut4-R	5'-GTCATAGAACCTTTTGCCCATAAAG	Reverse SOEing primer to make a Rot $Q^{48}A$ mutant. Use with primer 313.
1124	Rot-Mut5-F	5'-GGTTCTATGACGGCAGCAGAAATGGAC	Forward SOEing primer to make a Rot $L^{54}A/K^{55}A$ mutant. Use with primer 311.
1125	Rot-Mut5-R	5'-GTCCATTTCTGCTGCCGTCATAGAACC	Reverse SOEing primer to make a Rot $L^{54}A/K^{55}A$ mutant. Use with primer 313.
1126	Rot-Mut6-F	5'-GATTTGTTGAAGCAGCAGCAGCAGCAGCAGCAGCAA CGTATAATAATTTAG	Forward SOEing primer to make a Rot $K^{64}A/P^{65}A/Y^{66}A/$ $K^{67}A/R^{68}A/T^{69}A/R^{70}A$ mutant. Use with primer 311.
1127	Rot-Mut6-R	5'-CTAAATTATTATACGTTGCTGCTGCTGCTGCTGCT GCTGCTTCAACAAATC	Reverse SOEing primer to make a Rot $K^{64}A/P^{65}A/Y^{66}A/$ $K^{67}A/R^{68}A/T^{69}A/R^{70}A$ mutant. Use with primer 313.
1128	Rot-Mut7-F	5'-CGAGAGCATATAATGCATTAGTTGAATTAG	Forward SOEing primer to make a Rot $T^{71}A/N^{74}A$ mutant. Use with primer 311.

1129	Rot-Mut7-R	5'-CTAATTCAACTAATGCATTATATGCTCTCG	Forward SOEing primer to make a Rot $T^{71}A/N^{74}A$ mutant. Use with primer 313.
1132	Rot-Mut9-F	5'-GACGATGAAGCAACAGTTATTATTC	Forward SOEing primer to make a Rot $R^{91}A$ mutant. Use with primer 311.
1133	Rot-Mut9-R	5'-GAATAATAACTGTTGCTTCATCGTC	Reverse SOEing primer to make a Rot $R^{91}A$ mutant. Use with primer 313.
1137	Rot-Mut13-F	5'-GAAGAAATTGCAATTTTAGCAACTTTATGGC	Forward SOEing primer to make a Rot $L^{41}A/L^{44}A$ mutant. Use with primer 311.
1138	Rot-Mut13-R	5'-GCCATAAAGTTGCTAAAATTGCAATTTCTTC	Reverse SOEing primer to make a Rot $L^{41}A/L^{44}A$ mutant. Use with primer 313.
311	rot-6xHis-3'-RXhoI	5’-CCCCTCGAG-TTAGTGATGGTGATGGTGATG-CACAGCAATAATTGCGTTTAAAC	Reverse primer to clone rot into pOS1-P*lgt*
313	rot5'F-NdeI	5’-CCCC-CATATG-AAAAAAGTAAATAACGACACTG	Forward primer to clone *rot* downstream of the *lgt* promoter in the pOS1-P*lgt* plasmid.
270	hla P1-RT	5’- AAAAAACTGCTAGTTATTAGAACGAAAGG	qRT-PCR analysis of *hla*
271	hla P2-RT	5’- GGCCAGGCTAAACCACTTTTG	qRT-PCR analysis of *hla*
278	16S P1-RT	5’- TGAGATGTTGGGTTAAGTCCCGCA	qRT-PCR analysis of 16S rRNA
279	16S P2-RT	5’- CGGTTTCGCTGCCCTTTGTATTGT	qRT-PCR analysis of 16S rRNA
280	ssl7 P1-RT	5’- AACGTTAGCTAAAGCAACATTGGC	qRT-PCR analysis of *ssl7*
281	ssl7 P2-RT	5’- TTGCTTGAACTGCTTGGCCTTCTG	qRT-PCR analysis of *ssl7*
290	spA1P1-RT	5’- CAGCAAACCATGCAGATGCTA	qRT-PCR analysis of *spA*
291	spA2P2-RT	5’- GCTAATGATAATCCACCAAATACAGTTG	qRT-PCR analysis of *spA*
370	lukE-P1	5’-GAAATGGGGCGTTACTCAAA	qRT-PCR analysis of *lukE*
371	lukE-P2	5’-GAATGGCCAAATCATTCGTT	qRT-PCR analysis of *lukE*
305	pssl7-R-BIO	5’-BIO-CCCC-AGTACTATTCTCCCAATCTATTT	biotinylated primer for EMSA probe amplification
341	pssl7-F	5’-CCCC-CTGCAG-GCAGACTAGTAATTGTAGGG	EMSA probe amplification
736	plukED-F-BIO	5'-BIO-AAGTTTCACTTTCTTTCTATATAAAT	biotinylated primer for EMSA probe amplification
397	plukED-R	5'-CCC-CTGCAG-ATCTTCGTTTAACGGACAATAG	EMSA probe amplification

677 **Table 6.** Plasmids used in this study.

Name	Description	Resistance	Reference
pOS1sGFP-P*ssl7-sod*RBS	*ssl7* promoter and *sod* RBS driving *sgfp* expression	Cm	Benson et al., 2011
pJC1111	Suicide vector used for integration into the SaP-1 site	Cd	Geisinger et al., 2008
pJC1111 P*ssl7-sod*RBS-sGFP	*ssl7* promoter and *sod* RBS driving *sgfp* expression cloned into the pJC1111 suicide vector	Cd	This study
pRN7023	Vector encoding the SaP-1 integrase	Cm	Ruzin et al., 2001
pOS1P*lgt*	*lgt* promoter in an empty vector	Cm	Bubeck Wardenburg et al 2006
pOS1P*lgt rot*	*lgt* promoter driving *rot* expression	Cm	Benson et al., 2011
pOS1P*lgt rot* $F^{10}A/L^{13}A/Q^{14}A/T^{17}A$	*lgt* promoter driving *rot* $F^{10}A/L^{13}A/Q^{14}A/T^{17}A$ expression	Cm	This study
pOS1P*lgt rot* $S^{36}A/E^{38}A/E^{39}A$	*lgt* promoter driving *rot* $S^{36}A/E^{38}A/E^{39}A$ expression	Cm	This study
pOS1P*lgt rot* $Q^{48}A$	*lgt* promoter driving *rot* $Q^{48}A$ expression	Cm	This study
pOS1p*lgt rot* $L^{54}A/K^{55}A$	*lgt* promoter driving *rot* $L^{54}A/K^{55}A$ expression	Cm	This study
pOS1P*lgt rot* $K^{64}A/P^{65}A/Y^{66}A/K^{67}A/R^{68}A/T^{69}A/R^{70}A$	*lgt* promoter driving *rot* $K^{64}A/P^{65}A/Y^{66}A/K^{67}A/R^{68}A/T^{69}A/R^{70}A$ expression	Cm	This study
pOS1P*lgt rot* $T^{71}A/N^{74}A$	*lgt* promoter driving *rot* $T^{71}A$ /$N^{74}A$ expression	Cm	This study
pOS1P*lgt rot* $R^{91}A$	*lgt* promoter driving *rot* $R^{91}A$ expression	Cm	This study
pOS1P*lgt rot* $L^{41}A/L^{44}A$	*lgt* promoter driving *rot* $L^{41}A/L^{44}A$ expression	Cm	This study
pET41b *rot6xhis*	*rot* expression vector	Kan	Benson et al., 2012

678

679 **FIGURE LEGENDS**

680 **FIGURE 1.** Rot Structure. **(A)** The Rot dimer is shown in a ribbon representation from a
681 side view. Monomers are colored in either cyan or green. The chloride ion is represented as
682 a magenta sphere. **(B)** The sequence of the region in the crystal structure from residue 6 to
683 133 plus three residues from the 6 x His tag is shown with the secondary structure
684 elements, including five α-helices and a two-stranded β-sheet. The structural motifs are
685 color-coded: the dimerization core helices (α1, α2, and α5) in green, the Helix-Turn-Helix
686 (HTH) (α3 and α4) containing the Recognition Helix (RH) (α4) in magenta, and the wing
687 (β1 and β2) in dark blue. The underlined residues make dimerization contacts. Red
688 residues are predicted to make contact with protein-partners, purple residues non-specific
689 contact with DNA, and orange residues specific contact with DNA. **(C)** Structural motifs
690 listed in (B) are shown on the Rot monomer. **(D)** The Rot dimer is shown in a B-factor putty
691 representation where the thickness of a region is proportional to its local B-factor and thus
692 its flexibility.

693

694 **FIGURE 2.** Hydrophobic dimerization interface and hydrogen bonds in the Rot dimer. **(A)**
695 The surfaces of the Rot molecules. The two monomers in the Rot dimer are colored cyan
696 and green, respectively and the hydrophobic residues depicted in yellow. **(B)** Water-
697 mediated contacts span the Rot dimerization interface. The side chains of residues that
698 extend across the dimerization interface are colored in magenta. The key water molecules
699 that participate in dimerization are shown as small red spheres. **(C)** A close-up view of (B)
700 in which hydrogen bonds are shown as black dotted lines. **(D)** A close-up view of the

701 hydrogen bonds formed between the side chains of the symmetry-related Q^{124} from each
702 Rot monomer.
703
704 **FIGURE 3.** Surface charge distribution and sequence conservation among SarA family
705 members. **(A)** Electrostatic profiles of SarA family proteins. The electrostatic surface
706 potentials of each protein are colored by charge, with blue representing positive and red
707 negative charge. Proteins are oriented with their WHTH facing forward. Proteins are
708 depicted from most to least acidic isoelectric point (left to right, top to bottom). **(B)**
709 Sequence alignment of WHTH domains of SarA family members. The height of each letter in
710 the top portion of the figure represents the prevalence of that amino acid at the particular
711 position. **(C)** Sequence conservation of SarA family members projected onto Rot surface.
712 Each residue on the surface of Rot is colored according to sequence conservation, with blue
713 representing the most and red the least conserved. Sequence conservation was defined by
714 alignment generated by BLAST. Figure was generated by the ConSurf program (Ashkenazy
715 et al., 2010).
716
717 **FIGURE 4.** Prediction of domains important for Rot function. **(A)** Model of Rot/DNA
718 interaction. Rot dimer (cyan and green) are depicted as ribbons, while the DNA (brown)
719 backbones and bases are depicted as thin tubes with an overall transparent surface. The
720 side chains of Y^{66} and R^{91} are shown. **(B)** A zoomed in view of the modeled interaction at
721 the major and minor grooves. The side chains are shown for Y^{66} in the RH with the major
722 groove of DNA and R^{91} of the wing with the minor groove. **(C)** Optimal Docking Area (ODA)
723 analysis. ODA was used to predict interfaces for protein-protein interactions (Fernandez-

724 Recio et al., 2002). Red spheres indicate locations on the surface of Rot where protein
725 interactions are likely to occur. **(D)** Side chains are shown for residues predicted from the
726 ODA analysis to interact with protein partners.
727
728 **FIGURE 5.** Targeted Rot residues for site directed mutagenesis. **(A)** Residues altered to
729 generate mutant Rot proteins are shown in stick representation. Orange residues are
730 predicted to make specific contacts with DNA. Purple residues are predicted to make non-
731 specific contacts with DNA. Red residues are predicted to be involved in interactions with
732 protein partners. Distances between the Y^{66} residues and the R^{91} residues in the two
733 monomers are reported. **(B)** The WHTH region is shown in a close-up view with the side
734 chains of selected residues in stick representation. The chloride ion is shown as a red
735 sphere. **(C)** and **(D)** The HTH region is shown from two orientations. **(E)** Close-up view of
736 the region predicted by ODA to be involved in interaction with protein partners.
737
738 **FIGURE 6.** Mutant Rot proteins display functional defects. **(A)** Mutant *rot* alleles carried on
739 plasmid pOS1P*lgt* were transformed into an *S. aureus* reporter straining containing *sgfp*
740 under the control of the *ssl7* promoter, which is activated by Rot. Activation activity of Rot
741 mutants was assessed by GFP fluorescence in cultures grown to post-exponential phase.
742 Values represent the average of three independent experiments ± standard deviation (SD).
743 **(B)** Immunoblot analysis of α-toxin and Ssl7. *S. aureus* strain Newman was grown to post-
744 exponential phase. Exoproteins were collected, precipitated, separated by SDS-PAGE,
745 transferred to nitrocellulose, and probed with antibodies to indicated proteins.
746

747 **FIGURE 7.** Mutations in Rot differentially affect activation, repression, and DNA binding. **(A**
748 **– D)** Transcript levels of *ssL7* (A) and *spA* (B), which are activated by Rot, or *lukE* (C) and
749 *hla* (D), which are repressed by Rot, were quantified by qRT-PCR from strains containing
750 the wild type Rot or its mutant proteins. Transcript levels were quantified in units of
751 Relative Quantitation (RQ) and compared to that of the empty vector (Neg) or the wild type
752 Rot protein (WT). Data bars represent an average of 3 experiments ± SD. **(E – F)** EMSA
753 analysis of purified WT and mutant Rot proteins incubated with either the *ssl7* (E) or *lukED*
754 (F) promoters containing a biotin tag. Promoter DNA probes alone (Neg) or pre-incubated
755 with Rot-His proteins were separated by PAGE. DNA probes were visualized using
756 streptavidin DyLight. "P" denotes unbound DNA probe. "S" denotes shifted band resulting
757 from Rot-DNA complex. The asterisk denotes a non-specific band.

Figure 1

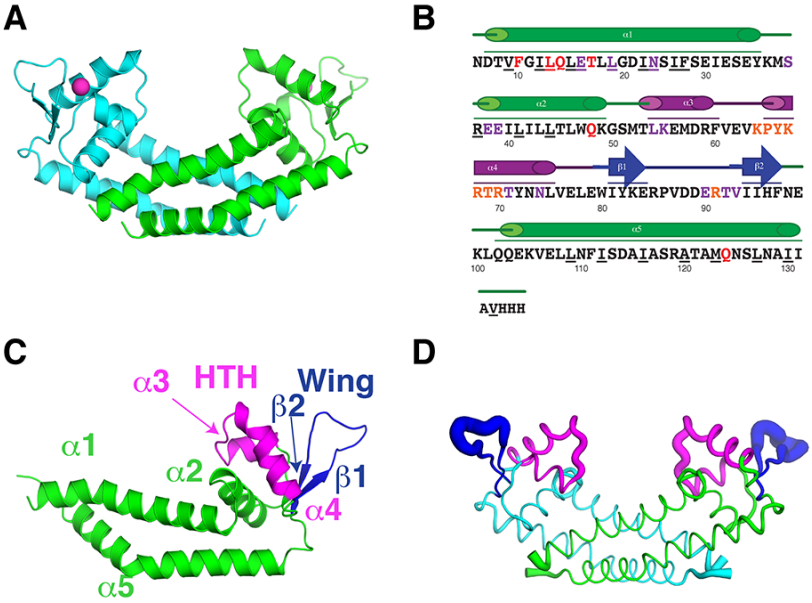

FIGURE 1. Rot Structure. **(A)** The Rot dimer is shown in a ribbon representation from a side view. Monomers are colored in either cyan or green. The chloride ion is represented as a magenta sphere. **(B)** The sequence of the region in the crystal structure from residue 6 to 133 plus three residues from the 6 x His tag is shown with the secondary structure elements, including five α-helices and a two-stranded β-sheet. The structural motifs are color-coded: the dimerization core helices (α1, α2, and α5) in green, the Helix-Turn-Helix (HTH) (α3 and α4) containing the Recognition Helix (RH) (α4) in magenta, and the wing (β1 and β2) in dark blue. The underlined residues make dimerization contacts. Red residues are predicted to make contact with protein-partners, purple residues non-specific contact with DNA, and orange residues specific contact with DNA. **(C)** Structural motifs listed in (B) are shown on the Rot monomer. **(D)** The Rot dimer is shown in a B-factor putty representation where the thickness of a region is proportional to its local B-factor and thus its flexibility.

Figure 2

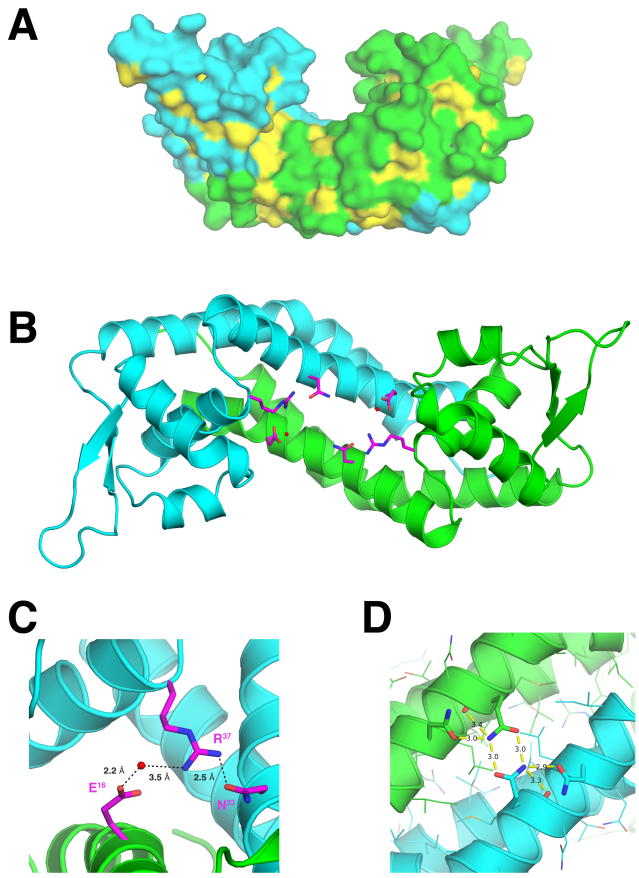

FIGURE 2. Hydrophobic dimerization interface and hydrogen bonds in the Rot dimer. **(A)** The surfaces of the Rot molecules. The two monomers in the Rot dimer are colored cyan and green, respectively and the hydrophobic residues depicted in yellow. **(B)** Water-mediated contacts span the Rot dimerization interface. The side chains of residues that extend across the dimerization interface are colored in magenta. The key water molecules that participate in dimerization are shown as small red spheres. **(C)** A close-up view of (B) in which hydrogen bonds are shown as black dotted lines. **(D)** A close-up view of the hydrogen bonds formed between the side chains of the symmetry-related Q^{124} from each Rot monomer.

Figure 3

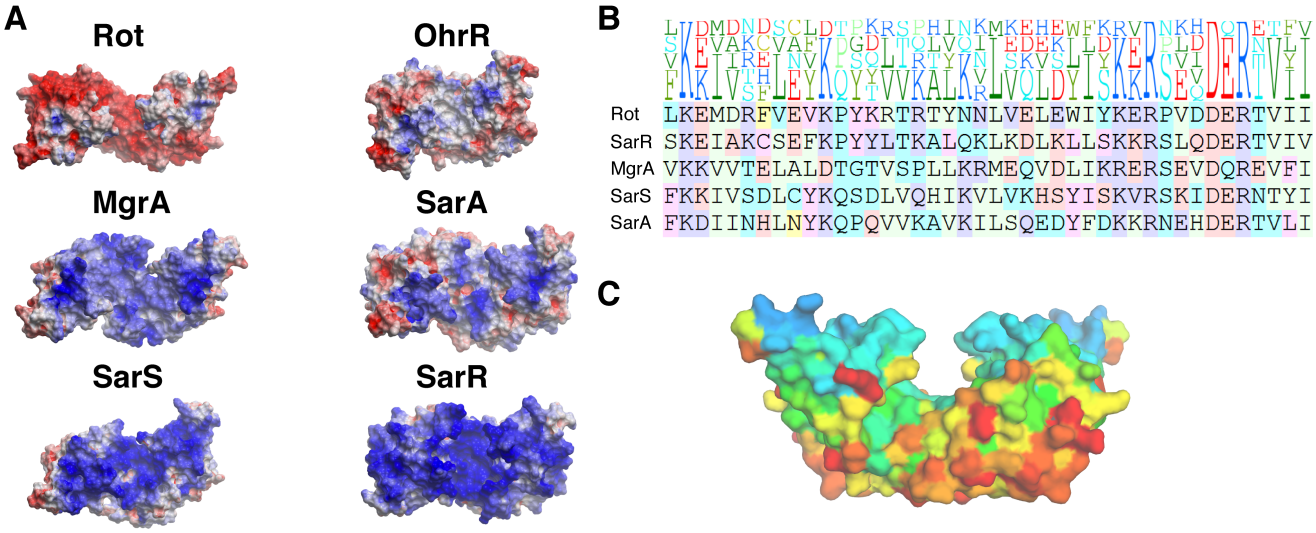

FIGURE 3. Surface charge distribution and sequence conservation among SarA family members. **(A)** Electrostatic profiles of SarA family proteins. The electrostatic surface potentials of each protein are colored by charge, with blue representing positive and red negative charge. Proteins are oriented with their WHTH facing forward. Proteins are depicted from most to least acidic isoelectric point (left to right, top to bottom). **(B)** Sequence alignment of WHTH domains of SarA family members. The height of each letter in the top portion of the figure represents the prevalence of that amino acid at the particular position. **(C)** Sequence conservation of SarA family members projected onto Rot surface. Each residue on the surface of Rot is colored according to sequence conservation, with blue representing the most and red the least conserved. Sequence conservation was defined by alignment generated by BLAST. Figure was generated by the ConSurf program (Ashkenazy et al., 2010).

Figure 4

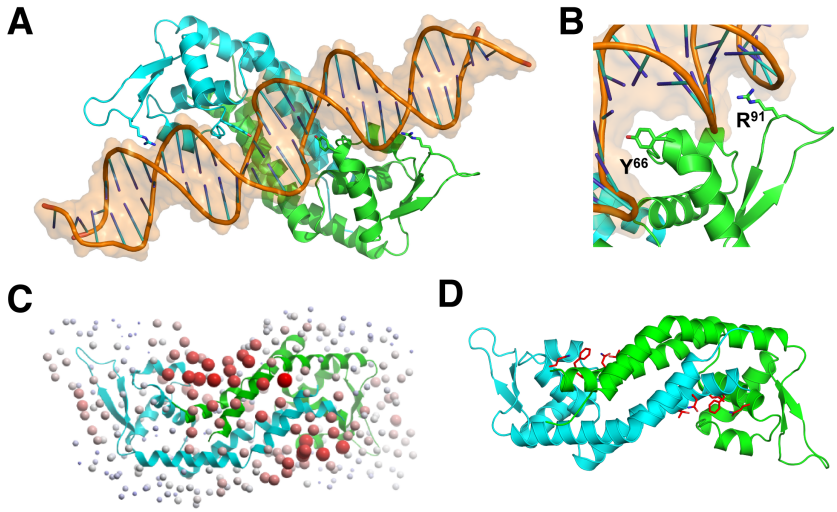

FIGURE 4. Prediction of domains important for Rot function. **(A)** Model of Rot/DNA interaction. Rot dimer (cyan and green) are depicted as ribbons, while the DNA (brown) backbones and bases are depicted as thin tubes with an overall transparent surface. The side chains of Y^{66} and R^{91} are shown. **(B)** A zoomed in view of the modeled interaction at the major and minor grooves. The side chains are shown for Y^{66} in the RH with the major groove of DNA and R^{91} of the wing with the minor groove. **(C)** Optimal Docking Area (ODA) analysis. ODA was used to predict interfaces for protein-protein interactions (Fernandez-Recio et al., 2002). Red spheres indicate locations on the surface of Rot where protein interactions are likely to occur. **(D)** Side chains are shown for residues predicted from the ODA analysis to interact with protein partners.

Figure 5

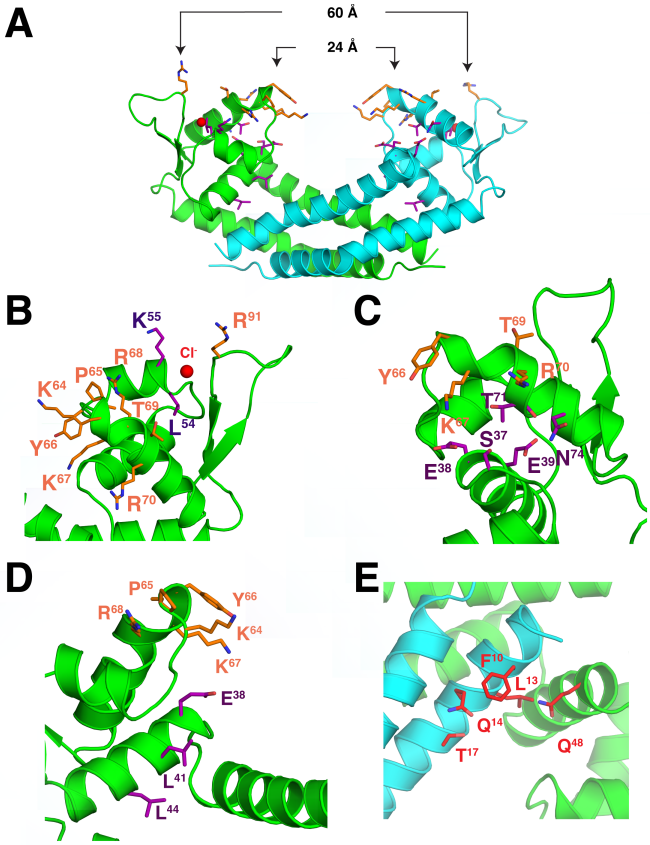

FIGURE 5. Targeted Rot residues for site directed mutagenesis. **(A)** Residues altered to generate mutant Rot proteins are shown in stick representation. Orange residues are predicted to make specific contacts with DNA. Purple residues are predicted to make non-specific contacts with DNA. Red residues are predicted to be involved in interactions with protein partners. Distances between the Y^{66} residues and the R^{91} residues in the two monomers are reported. **(B)** The WHTH region is shown in a close-up view with the side chains of selected residues in stick representation. The chloride ion is shown as a red sphere. **(C)** and **(D)** The HTH region is shown from two orientations. **(E)** Close-up view of the region predicted by ODA to be involved in interaction with protein partners.

Figure 6

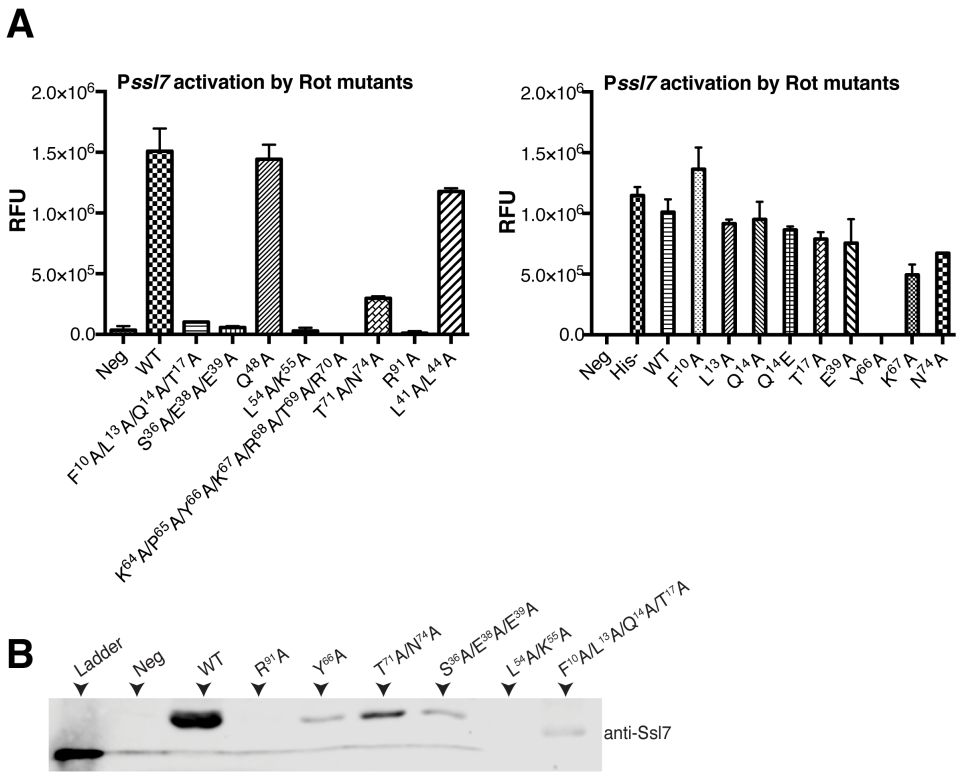

FIGURE 6. Mutant Rot proteins display functional defects. **(A)** Mutant *rot* alleles carried on plasmid pOS1P*lgt* were transformed into an *S. aureus* reporter straining containing *sgfp* under the control of the *ssl7* promoter, which is activated by Rot. Activation activity of Rot mutants was assessed by GFP fluorescence in cultures grown to post-exponential phase. Values represent the average of three independent experiments ± standard deviation (SD). **(B)** Immunoblot analysis of α-toxin and Ssl7. *S. aureus* strain Newman was grown to post-expontential phase. Exoproteins were collected, precipitated, separated by SDS-PAGE, transferred to nitrocellulose, and probed with antibodies to indicated proteins.

Figure 7

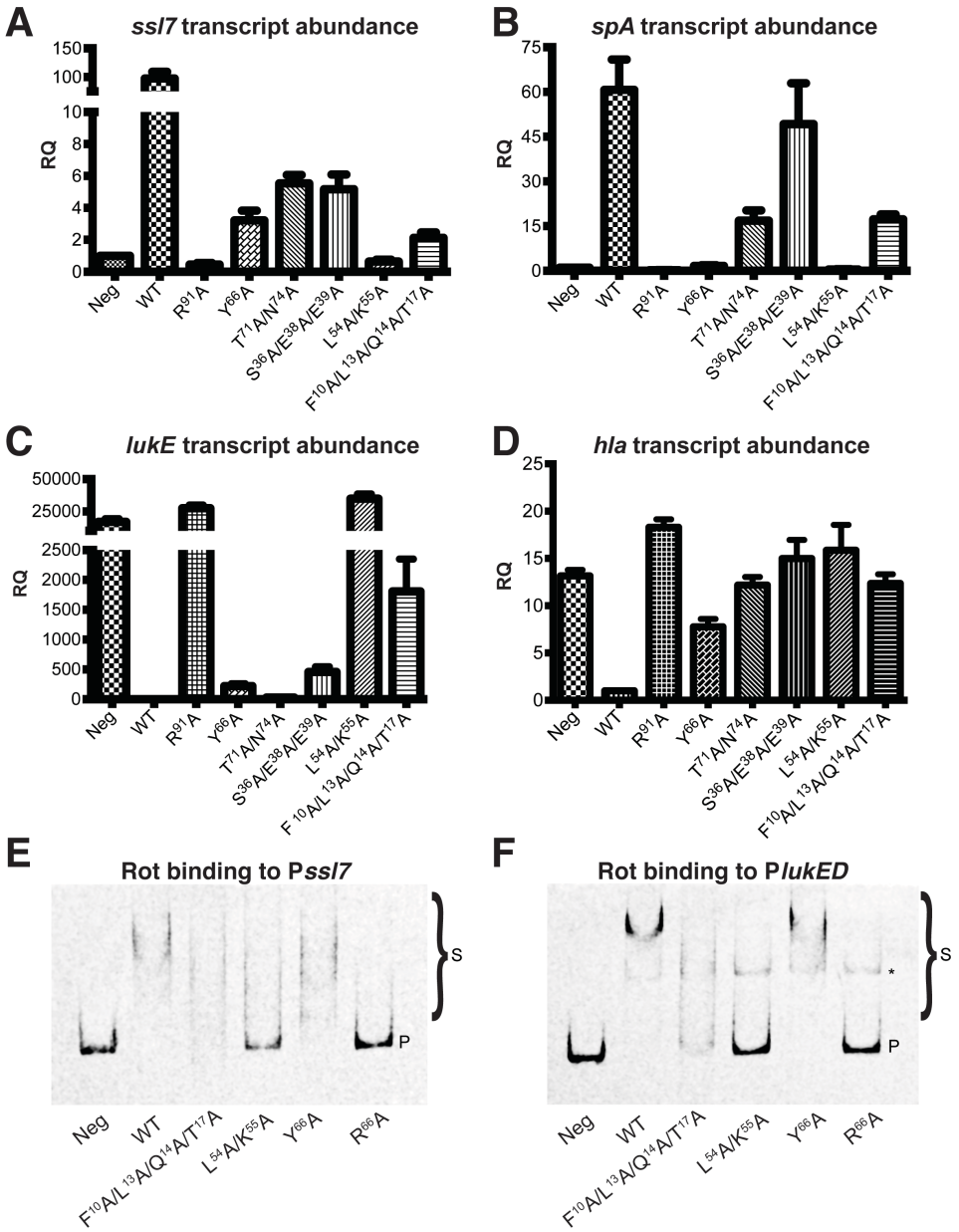

FIGURE 7. Mutations in Rot differentially affect activation, repression, and DNA binding. **(A – D)** Transcript levels of *ssL7* (A) and *spA* (B), which are activated by Rot, or *lukE* (C) and *hla* (D), which are repressed by Rot, were quantified by qRT-PCR from strains containing the wild type Rot or its mutant proteins. Transcript levels were quantified in units of Relative Quantitation (RQ) and compared to that of the empty vector (Neg) or the wild type Rot protein (WT). Data bars represent an average of 3 experiments ± SD. **(E – F)** EMSA analysis of purified WT and mutant Rot proteins incubated with either the *ssl7* (E) or *lukED* (F) promoters containing a biotin tag. Promoter DNA probes alone (Neg) or pre-incubated with Rot-His proteins were separated by PAGE. DNA probes were visualized using streptavidin DyLight. “P” denotes unbound DNA probe. “S” denotes shifted band resulting from Rot-DNA complex. The asterisk denotes a non-specific band.